Journal of Power Sources 239 (2013) 132–143

Contents lists available at SciVerse ScienceDirect

Journal of Power Sources

journal homepage: www.elsevier.com/locate/jpowsour

Evaluation and electrochemical analyses of cathodes for lithium-air batteries

James Adams*, Mohan Karulkar, Venkataramani Anandan

Ford Motor Company, 2101 Village Road, MD 3179, Dearborn, MI 48121, USA

HIGHLIGHTS

- Engineered cathodes to produce significant performance while operating on air.
- Measured peak power, specific energy, and discharge capacity of cathodes.
- Discharge reaction is controlled by kinetic, ionic and mass transfer resistances.
- Impedances should be measured during discharge, not OCV.
- Impedances depend on the magnitude of the discharge current density.

ARTICLE INFO

Article history:
Received 31 January 2013
Received in revised form
22 March 2013
Accepted 23 March 2013
Available online 3 April 2013

Keywords:
Lithium air
Battery
Power
Impedance

ABSTRACT

The performance of cathodes for lithium-air cells is evaluated from an automotive perspective. Unique aspects of this work include the following. Novel cathode structures are fabricated to improve cell performance operating on air. Convective air flow, critical to automotive operation, is used to evaluate cathode performance, and techniques to mitigate the resulting solvent evaporation from the electrolyte are discussed. The peak power is measured using the standard USABC test procedure, a benchmark for evaluating automotive performance. The importance of the kinetic, ionic, and mass transfer impedances as a function of discharge current density is identified using Tafel slopes, reaction orders, and electrochemical impedance spectroscopy (EIS) data. The distinct processes in the EIS data are identified as the anode–separator interface and the cathode. For the lithium-air cells used in this work, the discharge is controlled by a combination of the ionic transfer impedance at the anode–separator interface and the kinetic and mass transfer impedances in the cathode. Finally, impedance data establish the importance of performing EIS during discharge, not at open circuit voltage, to accurately determine the processes controlling the discharge reaction. The implication of these results to automotive applications for lithium-air batteries is discussed.

© 2013 Elsevier B.V. All rights reserved.

1. Introduction

Substantial improvement in the performance of rechargeable batteries is required for widespread commercialization of electric vehicles (EV). State-of-the-art (SOA) lithium-ion technology using graphitic carbon and inorganic oxides delivers ~180 Wh kg^{-1}, and a two-fold improvement is likely the most that can be expected [1]. Lithium-air batteries are an attractive alternative, harnessing the energy created by the reaction of a lithium metal anode and an oxygen-accessible porous cathode [1–8]. Although the lithium–oxygen couple has a high theoretical specific energy of 12 kWh kg^{-1}, many challenges must be solved to develop a lithium-air cell that simultaneously meets the energy, power, and cost targets necessary for application in an EV.

In spite of the recent increase in research on lithium-oxygen batteries in the areas of cathode capacity, catalysis, and the influence of electrolyte composition, three specific technical challenges remain to be solved before lithium-air batteries can be considered for commercial automotive applications. First, the lab-scale cell designs used for lithium-air research are not suitable for automotive applications because they are not amenable to high volume manufacturing and do not minimize mass and volume in order to maximize energy and power densities. Second, the cycle life of SOA lithium-air cells is at least two orders of magnitude below commercialization requirements. Third, SOA lithium-air cells achieve low discharge current densities, and thus low power densities, even when operating on pure oxygen.

* Corresponding author. Tel.: +1 313 594 0832; fax: +1 313 621 0646.
E-mail addresses: jadams23@ford.com (J. Adams), mkarulka@ford.com (M. Karulkar), vananda3@ford.com (V. Anandan).

0378-7753/$ – see front matter © 2013 Elsevier B.V. All rights reserved.
http://dx.doi.org/10.1016/j.jpowsour.2013.03.140

Proton exchange membrane (PEM) fuel cell experience has shown that air is the only technically viable option for an oxidant source in vehicles. Pure oxygen is difficult to store efficiently onboard the vehicle and complicates refueling, while onboard purification of oxygen from air requires excessive amounts of parasitic power. Regardless of the cell design, the power densities must be improved while operating on air, not pure oxygen. Using a bipolar plate design, for example, the power density must be increased by two orders of magnitude over SOA lithium-air cells [9] to achieve the long-term battery goals [10].

To address the challenges described above, a detailed understanding of the electrochemical processes occurring at the electrodes is required. The behavior of porous, air cathodes and the EIS analysis techniques used to study them have not yet been fully established for lithium-air cells, but are well documented in the PEM fuel cell literature [11–23]. In addition, the operating regimes (kinetic, ionic, and/or mass transfer) for lithium-air cells have not been identified, but are documented for PEM fuel cell cathodes using steady-state polarization data [12,18,20,24]. In contrast to fuel cells, limited EIS data for lithium-oxygen cells have been published in the literature. In these studies, the impedance was measured at OCV at intervals between discharge periods [25–27]. None of the above studies measured the impedance during discharge and the assignment of the impedance to cell processes was not performed.

This paper describes efforts to evaluate and improve the performance of lithium-air batteries for automotive applications. Using existing materials, different cathode fabrication techniques are employed to engineer the cathode structure for improved performance using convective air flow. In addition, experimental procedures are established to identify the operating regime and controlling impedances during discharge in lithium-air cells using electrochemical techniques such as EIS and polarization curves. Electrolytes based on carbonate solvents are used to minimize solvent evaporation during experiments using convective air flow. Although carbonate solvent decomposition during discharge in lithium-air batteries is now well established [28–30], stable solvents known to produce lithium peroxide during discharge, such as dimethoxyethane (DME), suffer excessive evaporation and loss of ionic conductivity when convective air flow is used. When using carbonate solvents, only the first discharge data are studied; no recharge or cycling is performed to minimize solvent decomposition effects. The results of this study apply only to the discharge reaction. Measured Tafel slopes and EIS data suggest that the controlling impedances during discharge are similar in both carbonate- and DME-based electrolytes, even though the discharge products are different. For the cathodes fabricated in this work, only kinetic resistance controls the discharge reaction at extremely low currents. At higher currents, the discharge reaction rate is controlled by kinetic, ionic, and mass transfer resistances.

2. Experimental

2.1. Cathode fabrication

Five different fabrication techniques were investigated: (1) soaked electrolyte separate cast (SC) cathodes; (2) soaked electrolyte dual cast (DC) cathodes; (3) embedded electrolyte DC cathodes; (4) room temperature ionic liquid (RTIL) embedded electrolyte DC cathodes; and (5) PTFE-calendered cathodes.

SC cathodes were made by casting a slurry of carbon (3.1 wt%, Super C45, TIMCAL, Ltd.), PVDF-HFP (4.7 wt%, Kynar Powerflex® LBG, Arkema, Inc.), and dibutyl phthalate (DBP) (9.7 wt%, Alfa Aesar) in acetone (82.5 wt%) on glass using a doctor blade, drying at room temperature, extracting the DBP using methanol, vacuum drying at room temperature, then soaking the cathode in electrolyte prior to use. The separator was cast in a distinct step from a solution of PVDF-HFP (13.4 wt%), DBP (12.4 wt%) in acetone (74.2 wt%), dried, extracted, vacuum dried, and soaked in electrolyte before use. DC cathodes were made by sequentially casting the cathode slurry followed by the separator slurry directly on top of the cathode (or vice versa), then dried, extracted, vacuum dried, and soaked in electrolyte before use. Embedded electrolyte DC cathodes were cast from a slurry of carbon (2.9 wt%), PVDF-HFP (4.3 wt%), acetone (76.0 wt%), and electrolyte (16.8 wt%); the separator solution was PVDF-HFP (13.0 wt%), acetone (56.5 wt%), and electrolyte (30.4 wt%). The embedded electrolyte DC cathodes were cast and dried in a glove box and used without further treatment. Soaked SC, soaked DC, and embedded DC cathodes had an average carbon loading of 1.9 mg cm^{-2}. SC cathodes had an average thickness of 90 μm, while DC cathodes had a cathode and total thickness of 64 μm and 100 μm, respectively.

PTFE-calendered cathodes were prepared as a free-standing film using Vulcan carbon as a conducting material and PTFE as a binder. Initially, 75 mg of PTFE emulsion (TFE 30, Electrochem Inc., MA) were added to a solution containing 4 ml of methanol and 4 ml of water, followed by an addition of 0.4 g of Vulcan carbon (Cabot, Cabot Corporation, MA). The resulting mixture was ultrasonicated (Branson Ultrasonics Corp, CT) for 1 h and dried overnight under vacuum at room temperature. The resulting powder contained 85 wt% carbon and 15 wt% PTFE binder. The dry powder was then wetted with 3–5 drops of methanol and placed between flat stainless steel plates. Using a hydraulic press (Carver, Inc., IN), a pressure of 3450 kPa was applied for 10 s, compressing the powder into a sheet. The sheet was peeled from the plates, folded, and pressed again at 13.8 MPa for 10 s. The folding and pressing process was then repeated at 20.7 MPa. Finally, the resulting sheet was rolled to the required thickness using stainless steel shims. Cathodes fabricated using this method had a thickness of 125 μm and a carbon loading of 6 mg cm^{-2}.

2.2. Electrolyte composition

Propylene carbonate (PC) and ethylene carbonate (EC) were purchased from Novolyte Technologies, Inc. The PC was treated with 4 Å molecular sieves prior to use to remove water contamination. 1,2 dimethoxyethane (DME) was purchased from Sigma–Aldrich Corp. The electrolyte salt lithium bis(trifluoromethylsulfonyl)imide (LiTFSI) and the RTIL 1-ethyl-3-methylimidazolium bis(trifluoromethylsulfonyl)imide (EMITFSI) were purchased from Sigma–Aldrich Corp. The electrolyte compositions used in this study were: (1) 1 M LiTFSI in DME; (2) 1 M LiTFSI in PC/EC (1:1 wt.); and (3) 0.5 M LiTFSI in EMITFSI.

2.3. Cell assembly

Swagelok® cells were used in all experiments. The Swagelok® cell consisted of a 12.7 mm Teflon union with the center bored through to 12.7 mm to allow the electrodes to move freely inside the union. The cathode side of the Swagelok® cell was fitted with a 12.7 mm stainless steel tube that served as the gas inlet and electrical connection. The anode side was fitted with a 12.7 mm solid stainless steel rod that served as the lithium metal anode support and electrical connection. In cell assembly, a 0.75 mm thick lithium foil, 8 mm in diameter was placed on the anode stainless steel rod, followed by separator-cathode (SC or DC), and finally a cathode current collector, consisting of a 12 mm diameter 60 × 60 mesh, 0.28 mm wire stainless steel screen. The current collector provided electrical contact between the cathode and the stainless steel tube. Cells were assembled under 88 kPa compression inside an argon-atmosphere glove box. The diameters for SC cathodes and

separators were 9 mm and 12 mm, respectively. For DC cathodes, 10 mm diameter separator/cathodes disks were used to prevent shorting between the anode and cathode. For PTFE cathodes, the separators were 12 mm diameter (Celgard 2400) and the cathodes were 9 mm in diameter. Except for the embedded electrolyte cathodes, both the separators and cathodes were soaked in electrolyte prior to assembly.

The cell could be operated in either dead-ended or flowing gas mode with an inlet pressure of 205 kPa; in flowing mode, the outlet pressure was 170 kPa. In flowing mode, a PC/EC solvent humidifier was used to eliminate solvent evaporation during discharge. The flow rate was adjusted by a needle valve and set to approximately 10 ml min^{-1}. Prior to operation, the cells were purged with operating gas for 5 min, and then equilibrated at open circuit for 2 h. Pure oxygen was fed from a gas cylinder. Laboratory air with a dew point of −40 °C was used for air experiments without further treatment. A 5% oxygen mixture was obtained by mixing laboratory air and nitrogen in the appropriate amounts; the gas mixture oxygen concentration was validated using a Model 755 Beckman oxygen analyzer. All experiments were conducted at a room temperature of 20 °C.

2.4. Experimental descriptions

2.4.1. Discharge capacity measurement

Cells were discharged in galvanostatic mode using current densities from 0.01 to 4 mA cm^{-2}. The discharge cutoff cell voltage was 2.0 V. A Solartron 1470E Multistat was used to control the discharge.

2.4.2. Peak power calculation

The maximum sustained power capability of a battery, termed peak power, was determined based on 30 s discharge pulses at various depths of discharge (DOD). This standard USABC test procedure does not measure the actual peak power of the battery, but calculates a value based on measurements taken during a baseline C/3 discharge rate at 80% depth of discharge [31]. A resistance was determined based on a measurement of $\Delta V/\Delta I$ between a base current just before the beginning of a 30 s high current pulse (V_1, I_1) and a time near the end of the 30 s high current pulse (V_2, I_2) and calculated as

$$R = \Delta V/\Delta I = (V_1 - V_2)/(I_1 - I_2) \quad (1)$$

Using this R value, the IR-free open circuit voltage was calculated as

$$V_{IR\ \mathrm{free}} = V - IR \quad (2)$$

where either (V, I) pair (base or high current) can be used for the calculation. The peak power capability was calculated (not measured) based on the voltage and current deliverable under load as

$$\mathrm{Peak\ Power} = \mathrm{Voltage_{load}} \times \mathrm{Current_{load}} \quad (3)$$

where

$$\mathrm{Voltage_{load}} = 2/3 \times V_{IR\ \mathrm{free}} \quad (4)$$

$$\mathrm{Current_{load}} = -\left(1/3 \times V_{IR\ \mathrm{free}}\right)\Big/R \quad (5)$$

Therefore

$$\mathrm{Peak\ Power} = (-2/9)\left(V_{IR\ \mathrm{free}^2}\right)\Big/R \quad (6)$$

In all cases, the peak power was determined at 80% DOD or the highest DOD attained in the experiment.

2.4.3. Solvent evaporation and humidification

Solvent evaporation tests using convective air flow were conducted in a cathode sample holder, constructed from a 12.7 mm (0.5 in) O.D. stainless steel tube approximately 75 mm long that could be easily removed and reinstalled by using Swagelok® fittings. A layered assembly of a 10 mil thick PTFE sheet, a cathode sample, and finally a 30 × 30 mesh stainless steel screen placed on top of the cathode was slid into the stainless steel tube; the PTFE helped the cathode slide into the tube without tearing or bunching. The screen acted to securely hold the cathode next to the PTFE and the tube wall, allowing solvent evaporation from only the screen side of the cathode. The screen had approximately a 50% opening. The air pressure was controlled using a single stage pressure reducing regulator at the inlet and a single stage back pressure regulator at the outlet. The inlet pressure was fixed at 205 kPa for all experiments; the outlet pressure was either 170 kPa or ambient atmospheric pressure. A ball valve was used to switch the air flow on and off; a needle valve was used to control the air flow rate between 10 and 60 ml min^{-1}. Samples were exposed to varying operating conditions and periodically weighed to measure the amount of solvent evaporation.

The solvent humidifier was a modified water humidifier from Fuel Cells Technologies. A stainless steel sparger was connected to the air inlet inside the humidifier and placed on the bottom in order to maximize gas to liquid contact time. The humidifier was filled with only the solvent(s) used in the electrolyte. The head space above the solvent level accounted for approximately three-fourths of the internal volume of the humidifier.

2.4.4. Electrochemical impedance spectroscopy (EIS)

A Solartron 1470E Multistat was used in conjunction with a 1455 FRA unit installed in a 1400 chassis to collect the cell impedance data. During impedance measurements, the lithium-air cells were operated in galvanostatic mode at a discharge current density of 0.1 mA cm^{-2}, unless otherwise noted. The AC amplitude was set at 10% of the galvanostatic discharge current density, and the frequency range was 1 mHz–1 MHz. All other parameters were left in their default values.

A graphical interpretation of the Bode and Nyquist plots, shown in Fig. 1, was used as an alternative to equivalent circuit modeling [32]. From the Nyquist plot, the shape of the locus of points suggests possible governing mechanisms. A semicircle corresponds to an activation-energy-controlled process with the diameter of the semicircle corresponding to the process resistance. Multiple peaks indicate multiple processes with distinct time constants. The asymptotic limit of the real part of the impedance at high frequencies is generally associated with the electrolyte impedance (R_e). At low frequencies, the asymptotic limit of the real part of the impedance is the total impedance (R_t) in the overall process. From the Bode plot, differences in the plateau values of the real impedance correspond to distinct process impedances, while the imaginary impedance reaches a local minimum at a characteristic frequency related to a distinct process. This characteristic frequency is related to the capacitance of the process. As in the Nyquist plot, the high and low frequency asymptotic limits of the real part of the impedance are the electrolyte and total impedances, respectively, in the process. If desired, the impedance and capacitance values can be used to construct an equivalent RC circuit representing the overall process. For verification of the graphical interpretation, an equivalent circuit model fit to the data using commercial software is also presented.

2.4.5. Tafel slopes and reaction orders

Steady state polarization data were measured during discharge under galvanostatic control; steady state was usually achieved in

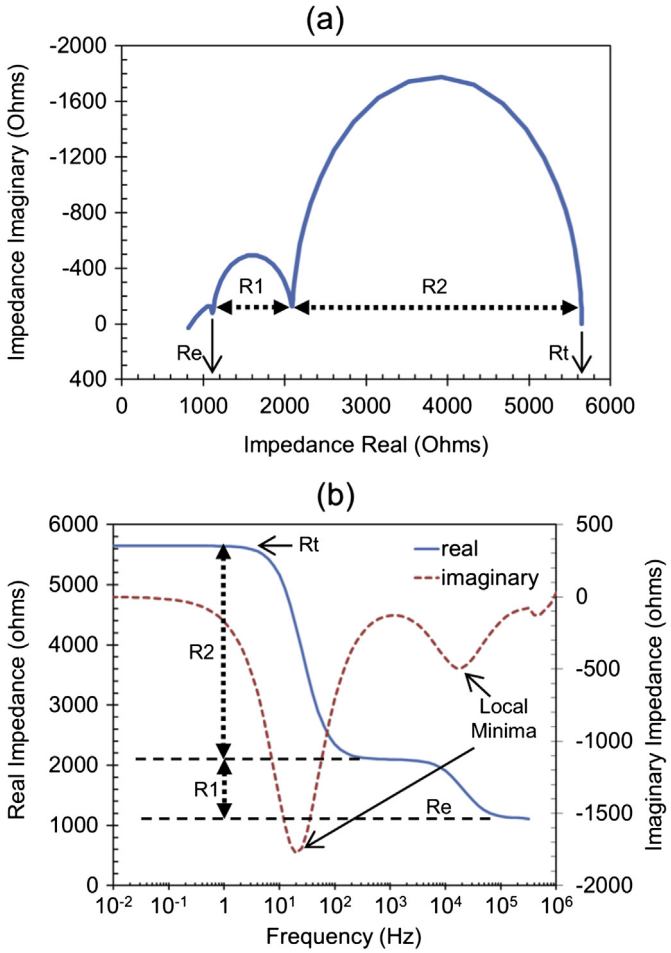

Fig. 1. Process information available from (a) Nyquist and (b) Bode plots.

less than 3 min of discharge. Tafel slopes were obtained by plotting cell voltage (not corrected for *IR* drop) vs. the logarithm of current. Reaction orders were estimated from the slopes of plots of logarithm of current vs. logarithm of the partial pressure of oxygen at constant voltage. Cell voltages of 2.72 V and 2.40 V were chosen for the low and high current determination of reaction orders, respectively. The partial pressure of oxygen was varied by changing the cell operating pressure using pure oxygen and air.

3. Results

3.1. Solvent evaporation and humidification

3.1.1. Evaporation without humidifier

The evaporation of solvent without a solvent humidifier from soaked DC cathodes using 1 M LiTFSI in PC/EC (1:1 wt.) with back pressure and convective air flow is shown in Fig. 2. The percent solvent loss is greater than 100% due to errors in estimating the initial amount of solvent in the cathode. The rate of solvent evaporation, i.e., the slope of the line segments for the different experimental conditions, is dependent on the back pressure and the air flow rate, as shown by the changes in the slopes. The percent solvent loss is significantly lower with back pressure, even with convective air flow (condition #1). Because the vapor pressure of the solvent (P_{vap}) is a function of only the temperature, higher operating pressures (P_{tot}) result in a lower equilibrium solvent fraction in air (P_{vap}/P_{tot} is smaller). As the convective air flow rate increases from 10 to 60 ml min^{-1}, the evaporation rate increases as

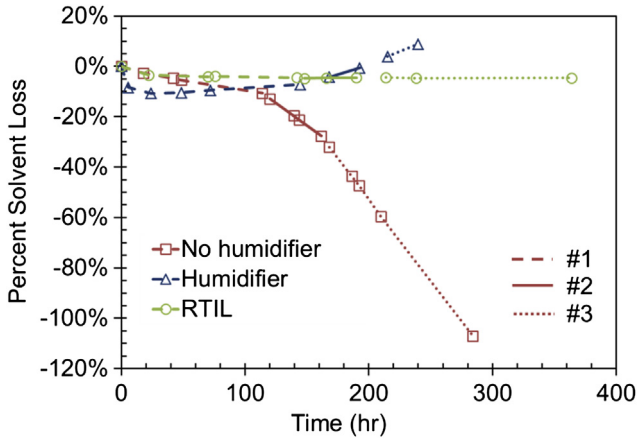

Fig. 2. Percent solvent loss from dual cast cathodes under pressurized air flow. Conditions: #1 – 205 kPa inlet, 170 kPa outlet, 10 ml min^{-1}; #2 – 205 kPa inlet, 170 kPa outlet, 60 ml min^{-1}; #3 – 205 kPa inlet, 101 kPa outlet, 60 ml min^{-1}.

reflected by the increase in the slope (condition #2). Finally, reducing the back pressure to ambient pressure at approximately constant air flow rate increases the evaporation rate due to the higher equilibrium solvent fraction in air (condition #3). These results suggest that operating pressure could be significant in controlling solvent evaporation from lithium-air cathodes.

3.1.2. Evaporation with humidifier

The evaporation of solvent from embedded electrolyte DC cathodes using 1 M LiTFSI in PC/EC (1:1 wt.) with back pressure and convective air flow with a solvent humidifier containing PC/EC (1:1 wt.) is also shown in Fig. 2. Following a 10% loss of solvent in the first day, the amount of solvent in the cathodes stabilizes, then slowly begins to increase, and eventually increases beyond the initial amount. The initial 10% loss of solvent is most likely due to the time necessary for purging solvent-free air in the test setup with solvent-laden air from the humidifier. The amount of solvent in the cathode increases with an increase in air flow rate and also when the back pressure is reduced to ambient pressure. These results show that the humidifier is robust in maintaining the solvent content of the cathodes over a variety of different operating conditions and is necessary to enable the use of convective air flow during discharge experiments.

3.1.3. RTIL embedded DC cathode without humidifier

The evaporation of the room temperature ionic liquid EMITFSI containing 0.5 M LiTFSI from embedded electrolyte DC cathodes with back pressure and convective air flow without a solvent humidifier is also shown in Fig. 2. After a 3% loss in the first 24 h, the cumulative percent solvent loss in the next 340 h increases by only 1%. The loss attributed to solvent evaporation could be residual solvent from the cathode fabrication procedure or volatile impurities in the RTIL. Distinct from the dual cast cathodes described above using carbonate-based electrolytes, the rate of RTIL evaporation is independent of the back pressure and the air flow rate, as shown by the constant slope. These results suggest that RTILs could be an alternative to traditional lithium-ion solvents for eliminating solvent evaporation from lithium-air cathodes.

3.2. Cathode engineering

3.2.1. Discharge capacity

Engineering the cathode structure can improve the discharge capacity of cathodes, especially when operating on air; the data are

shown in Table 1 as a function of discharge current density. When operating on oxygen, the discharge capacity of DC cathodes, either soaked or embedded, is increased compared to SC cathodes across the entire range of discharge current densities. The discharge capacities of soaked and embedded DC cathodes operating on oxygen are the same at all discharge current densities. When operating on air without flow, the discharge capacities of the DC cathodes decrease, as expected due to the lower oxygen concentration, but the decrease is much less in embedded DC cathodes compared to soaked DC, especially at higher current densities. When convective air flow is used, the discharge capacities of embedded DC cathodes are almost equivalent to pure oxygen performance, even at the higher current densities. These data show that through the use of two simple cathode fabrication modifications, sequentially casting the cathode followed by the separator (dual cast) and pre-mixing the electrolyte (embedded electrolyte) rather than post-soaking the cathode, the discharge capacity of cathodes using convective air flow can be equivalent to that using pure oxygen.

The large improvement in discharge capacity seen for the embedded electrolyte DC cathodes indicates better utilization of cathode materials, likely a result of better distribution of electrolyte within the cathode and less pore flooding by electrolyte. By incorporating electrolyte into the cathode during slurry mixing, a more homogeneous distribution is obtained than from soaking a dry cathode before use. From an automotive standpoint, this is an important achievement because it points directly to more feasible automotive operating conditions for a lithium-air battery.

In addition to the PVDF-HFP based DC cathodes, an entirely new cathode structure is engineered based on PTFE and carbon. PTFE-calendered cathodes utilize a DME-based electrolyte. DME is incompatible with the PVDF-based cathodes, causing them to disassemble. The discharge capacity as a function of discharge current density is shown at the bottom of Table 1. Although the discharge capacity is initially lower at 0.1 mA cm^{-2}, the PTFE cathodes yield discharge capacities twice that of embedded electrolyte DC cathodes at discharge current densities greater than 1 mA cm^{-2}. In addition, a substantial discharge capacity of 200 mAh g^{-1} carbon is obtained with the PTFE cathodes at a discharge current density of 4 mA cm^{-2}, which is not possible with embedded electrolyte DC cathodes.

The production of Li_2O_2 in PTFE cathodes during discharge is confirmed by XRD analysis, as shown in Fig. 3. No Li_2O_2 is observed in the cathodes prior to discharge, but is readily detected following discharge. In addition, the Li_2O_2 is recycled during charge, as noted by the lack of peaks in the charged cathodes. The PTFE cathodes support at least 15 discharge/charge cycles; however, cycle life is not the main purpose of this work. No Li_2O_2 is detected in any of the carbonate solvent-based DC cathodes after discharge.

The type of electrolyte used in the DC cathodes impacts the performance. In an effort to replace carbonate solvent-based electrolytes, the RTIL EMITFSI is used with 0.5 M LiTFSI to form embedded electrolyte DC cathodes. The performance of these cathodes is very poor. At a discharge current density of 0.01 mA cm^{-2}, the RTIL embedded DC cathodes show a discharge capacity of approximately 500 mAh g^{-1} carbon. This current density is two orders of magnitude lower compared to embedded DC and PTFE cathodes at the same discharge capacity. While not remarkable, these results suggest that RTILs may provide an alternative to carbonate-based electrolytes if some fundamental problems can be solved to improve performance.

Table 1
Discharge capacities (mAh g^{-1} carbon) of cathodes using different operating gases and discharge currents.

Cathode	Operating gas	Discharge current (mA cm^{-2})			
		0.1	0.4	0.7	1
Soaked SC	O_2	1680	770	570	430
Soaked DC	O_2	2160	1330	880	630
Embedded DC	O_2	2330	1340	740	570
Soaked DC	Air, no flow	1620	370	170	60
Embedded DC	Air, no flow	1530	940	450	260
Embedded DC	Air, flow	–	1380	690	530
		0.1	**1**	**2**	**4**
PTFE calendered	O_2	1100	1300	600	200

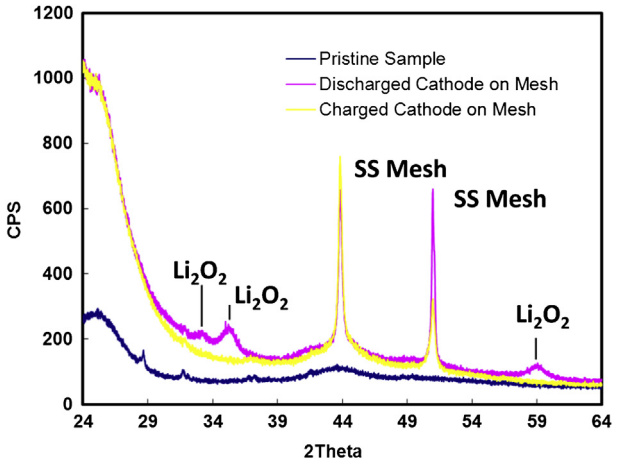

Fig. 3. XRD of PTFE cathodes before discharge, after discharge, and after charge.

3.2.2. Specific energy and peak power

The baseline C/3 discharge rates and the high current pulses used to calculate the specific energy and the peak power, respectively, are shown in Table 2 for selected cathodes. A median discharge voltage of 2.4 V is used to calculate the specific energy for all cathodes. The trends in the peak power and specific energy data are similar to those observed in the discharge capacity data. When operating on pure oxygen, dual cast cathodes have higher peak powers and specific energies than soaked SC cathodes. When operating on air without flow, embedded DC cathodes have an equivalent peak power, but a somewhat reduced specific energy, compared to soaked DC cathodes operating on pure oxygen. When convective air flow is used, the peak power of embedded DC cathodes dramatically increases. However, because the C/3 discharge rate is almost doubled using convective air flow, the specific energy is substantially reduced.

The discharge capacity, specific energy, and peak power data demonstrate the importance of the cathode structure in achieving performance goals. In addition, operation of lithium-air cells with convective air flow is demonstrated and performance can be significantly improved by engineering the cathode.

3.3. Tafel analysis and reaction orders

Typical polarization curves used to calculate Tafel slopes are shown in Fig. 4. Two different cathode/electrolyte systems are shown, PTFE-calendered cathodes soaked in a DME-based electrolyte and embedded electrolyte DC cathodes using a PC/EC-based electrolyte. Two linear regions are clearly visible for both types of cathodes; the low and high current regions are less than and greater than 0.04 mA (0.08 mA cm^{-2}), respectively.

The average Tafel slopes in the low and high current regions for embedded electrolyte DC cathodes and PTFE-calendered cathodes are shown in Fig. 5. The average Tafel slope in the low current

Table 2
Specific energy and peak power of various cathodes using different operating gases.

Electrode	Operating gas	C/3 baseline current density (mA cm^{-2})	High. pulse current density (mA cm^{-2})	C/3 Disch. capacity (mAh g^{-1} carbon)	Peak power (W kg^{-1} carbon)	Specific energy (Wh kg^{-1} carbon)
Soaked SC	Pure O_2, no flow	0.46	1.38	700	2550	1680
Soaked DC	Pure O_2, no flow	0.58	1.74	1100	3150	2640
	Air, no flow	0.54	–	300	–	720
Embedded DC	Pure O_2, no flow	0.56	–	1000	–	2400
	Air, no flow	0.40	0.80	900	3130	2160
	Air, flow	1.08	2.16	500	4380	1200

region is approximately 119 mV per decade, indicating the discharge reaction is under only kinetic control with one electron transfer in the rate-determining step (RDS). The Tafel slope is equivalent for cathodes operating on pure oxygen or air, as would be expected for such low discharge currents. At high currents, the average Tafel slope is approximately 463 mV per decade, which is four times the low current slope, indicating that kinetic, ionic transfer, and mass transfer resistances are all important.

As noted in Section 3.2.1, the PTFE cathodes using the DME-based electrolyte produce Li_2O_2 on discharge, which is reversibly converted back to lithium during charge. In contrast, the embedded DC cathodes using the carbonate-based electrolytes do not produce a reversible discharge product. Although the discharge products are different for these cathode-electrolyte systems, the Tafel slopes are nearly equivalent in both the low and high current regions. The equivalent Tafel slopes suggest that the rate controlling mechanism during discharge is the same in both the reversible (PTFE-DME) and the irreversible (embedded DC-PC/EC) cathode-electrolyte systems. This is an important result because it strongly suggests that the impedances controlling the discharge identified in the EIS data described in Section 3.4 may be independent of the discharge products formed.

The reaction orders for oxygen for the discharge reaction in embedded electrolyte DC cathodes are shown in Fig. 6. At low current densities, the slope indicates that the oxygen reaction order is 0.8, close to the value of 1.0 predicted by theory for discharge in the kinetically controlled region. At high current densities, the reaction order for oxygen is very close to 0.5, which is consistent with discharge in the kinetic, ionic transfer, and mass transfer controlled region. At the discharge current densities used in the majority of experiments in this work, the discharge reaction is controlled by kinetic, ionic, and mass transfer resistances.

3.4. EIS analysis

Graphical analysis of EIS data provides additional data to help interpret the experimental results. Three experimental areas are analyzed. First, the active process elements in the lithium-air cell are identified and an equivalent circuit for the lithium-air cell presented. Second, the effects of the cathode fabrication technique and the operating gas on the cell impedances are explored. Third, the differences in impedance data taken at OCV and during discharge are compared. Unless specified otherwise, all impedance data are measured during a constant current discharge.

3.4.1. Identification of process elements

A series resistance is present in all impedance spectra for all cells, which includes contributions from the electrolyte, electrical cables, etc. This resistance (R_e) is directly related to the electrolyte composition, as shown in Fig. 7, where the impedance results for two electrolyte salt concentrations, 1.0 M LiTFSI and 0.1 M LiTFSI in PC/EC, are compared in soaked DC cathodes. As expected, the R_e value increases by a factor of 2.5 when the salt concentration decreases from 1.0 M to 0.1 M LiTFSI.

In order to identify the active process elements in each cell, the imaginary impedances of separate cast and dual cast cathodes are shown in a Bode plot in Fig. 8. The soaked SC and DC cathodes show two distinct elements labeled #1 and #2, which represent a component or an interface in the cell. To help identify element #1, the imaginary impedance of a lithium–lithium cell using a PVDF-HFP separator is also shown. This cell contains only two lithium–separator interfaces. Because this cell displays only one minimum at the same frequency as element #1 in SC and DC cathodes, element #1 is identified as the lithium–separator interface with an impedance of R_1. Referring to Fig. 7, the R_1 values are 70% higher in the 0.1 M LiTFSI electrolyte compared to the 1.0 M LiTFSI electrolyte.

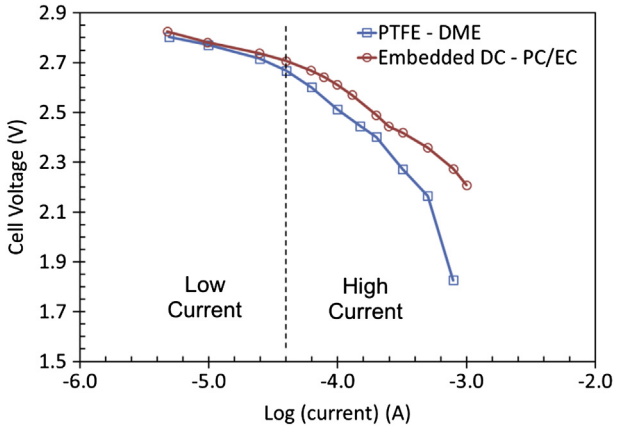

Fig. 4. Polarization curves for PTFE-DME and embedded DC-PC/EC cathodes.

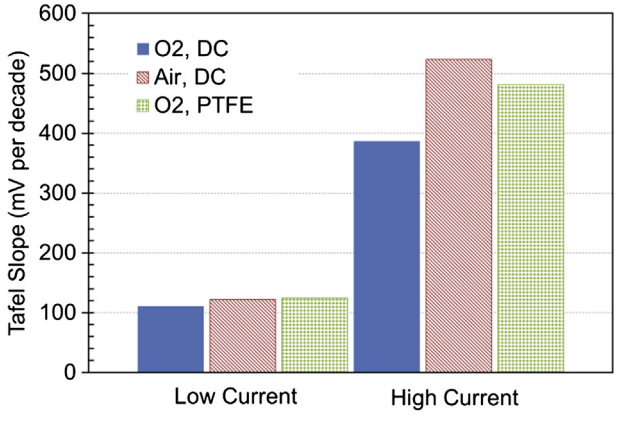

Fig. 5. Average Tafel slopes for embedded DC and PTFE-calendered cathodes at low and high currents.

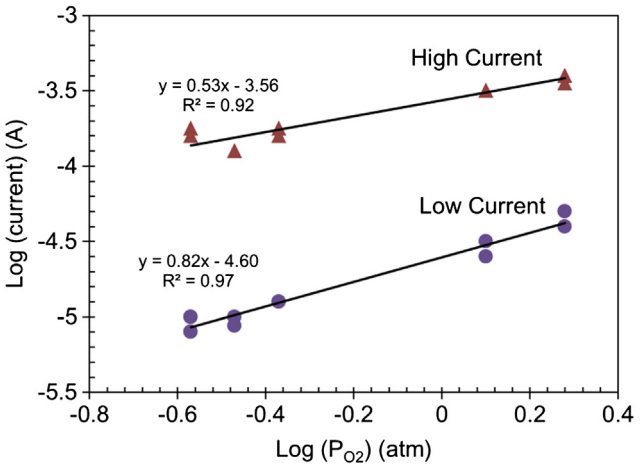

Fig. 6. Determination of oxygen reaction orders at low and high currents.

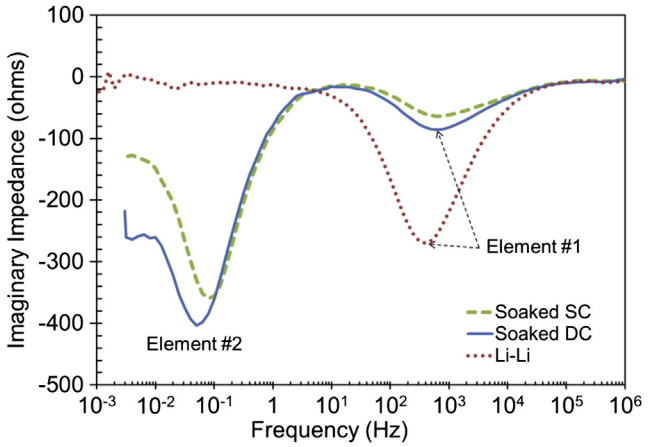

Fig. 8. Bode plot of imaginary impedances for soaked SC and DC cathodes and an Li–Li cell.

The higher R_1 impedance at the lower salt concentration is consistent with the R_1 impedance representing ionic transfer resistance at the lithium–separator interface.

Element #2 is identified as the cathode by examining the EIS data of embedded electrolyte DC cathodes measured at 100%, 21%, and 5% oxygen concentrations. Four impedance values representing the electrolyte (R_e), the lithium–separator interface (R_1), the impedance for element #2 (R_2), and the total cell impedance (R_t), are shown in Fig. 9. R_t is equal to the sum of R_e, R_1, and R_2. As expected, the R_e and R_1 values are not significantly affected by the oxygen concentration. The R_t value increases with decreasing oxygen concentration due only to an increase in the R_2 values. Based on these data, R_2 is assigned to the cathode.

The R_2 values for the two LiTFSI salt concentrations shown in Fig. 7 are equal, suggesting little or no ionic transfer resistance in the cathode. Therefore, the ionic transfer resistance identified in the Tafel slopes appears to arise mainly at the lithium anode–separator interface (R_1) for DC cathodes. If R_1 contains only the ionic resistance, then the kinetic and mass transfer resistances identified in the Tafel slopes must be present in the cathode (R_2).

An equivalent circuit model for a lithium-air cell with an embedded DC cathode during discharge is shown in Fig. 10. Because the data becomes noisy at low frequencies, only the data between 1 MHz and 0.03 Hz are used in developing the equivalent circuit model. The data suggest two process elements and a resistor in series with each other. The two process elements are each modeled initially as a resistor in parallel with a constant phase element (CPE). The CPE is modeled as $1/((j\omega)^{\alpha}Q)$. For a process with uniform activity, the CPE becomes an ideal capacitor with a value of $\alpha = 1$ and Q equals the capacitance (C). However, for a process with a non-uniform activity, the CPE is used in the model and $\alpha \neq 1$. The non-uniformity can result from surface heterogeneities in two dimensions and/or from variation in properties normal to the electrode surface.

A comparison of the experimental data to the equivalent circuit model is shown in the Nyquist plot in Fig. 10. The fitted values of α_1 and α_2 are 0.80 and 1.1, respectively. These α values compare very well to the values of α_1 and α_2 of 0.80 and 1.0, respectively, obtained graphically from a log–log plot of the imaginary impedance vs. frequency. Because α_2 is approximately 1.0, the second CPE is replaced by an ideal capacitor. The fit of the model using a CPE or capacitor for the cathode is equivalent, as indicated by the sum of squares. The fitted parameter value for Q_1 is 3.3 e^{-6} $s^{0.8}$ ohm^{-1} for CPE1, and the C_2 value is 3.1 mF. The C_2 capacitance compares very well to the value of 2.7 mF obtained graphically from the characteristic frequency of 0.5 Hz in the imaginary Bode plot. The fitted

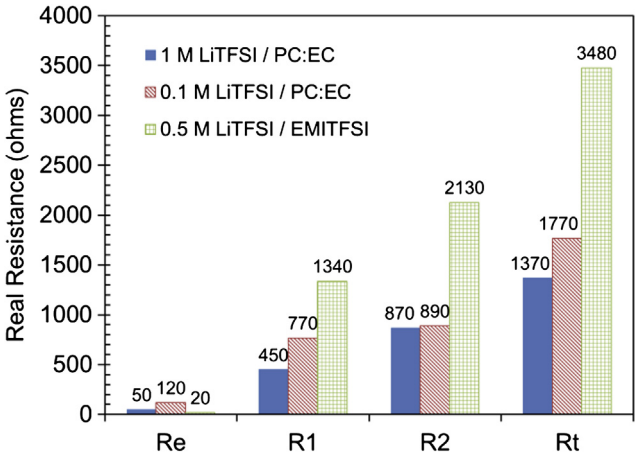

Fig. 7. Impedance data for cells using different electrolytes: 0.1 M and 1.0 M LiTFSI in PC:EC electrolytes in soaked DC cathodes; 0.5 M LiTFSI in EMITSI in embedded DC cathodes.

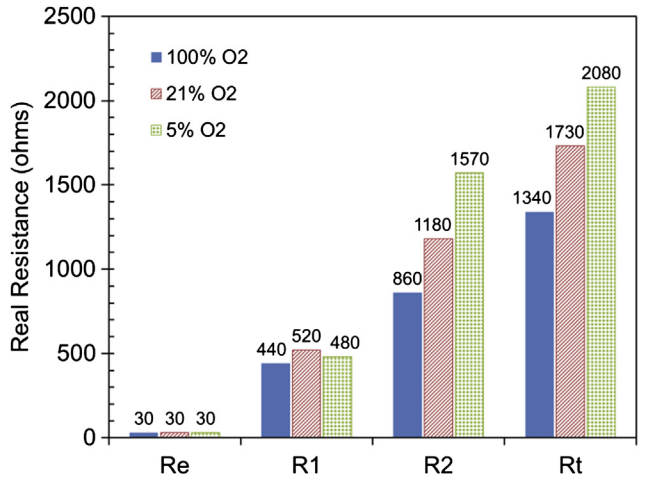

Fig. 9. Effect of oxygen concentration on impedance values for embedded DC cathodes.

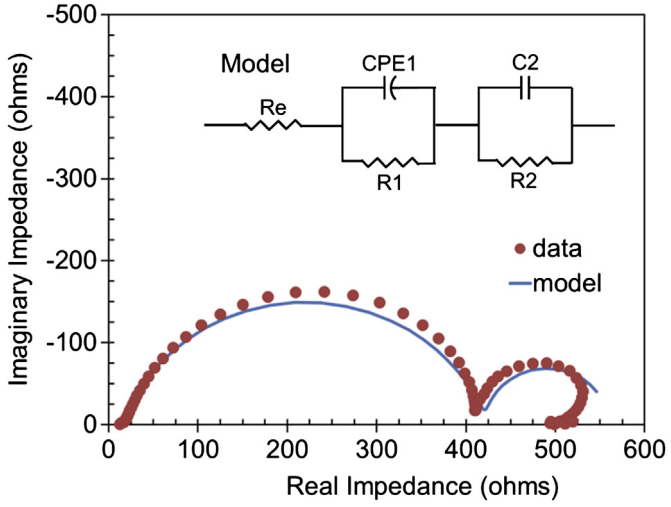

Fig. 10. Comparison of the experimental data to the equivalent circuit model for a lithium-air cell with an embedded DC cathode during discharge.

model parameter values for R_e, R_1, and R_2 are 16, 407, and 117 Ω, respectively, which also compare very well to the values obtained graphically from the real impedance plateaus in the Bode plot of 19, 391, and 120 Ω, respectively.

Using a value of 3 mF for the capacitance of the cathode, the capacitance per unit active area of electrode is estimated for embedded DC cathodes with a geometric area of the electrode of 0.5 cm^2, a carbon loading of 0.002 g carbon cm^{-2} geometric area, and an active area of 45 $m^2\ g^{-1}$ for the carbon particles. Using the above data, the capacitance per area of active electrode is estimated at 7 μF cm^{-2} active area. This value is somewhat lower than the range of 10–30 μF cm^{-2} active area from the literature [33,34], and suggests that these cathodes may be utilizing only a fraction of the available active area during discharge.

3.4.2. Cathode fabrication technique and operating gas

The different process impedances for cathodes fabricated by different techniques, including soaked DC, embedded electrolyte DC, and PTFE-calendered cathodes, are compared in Fig. 11 at low and high discharge current densities. The three operating gases are

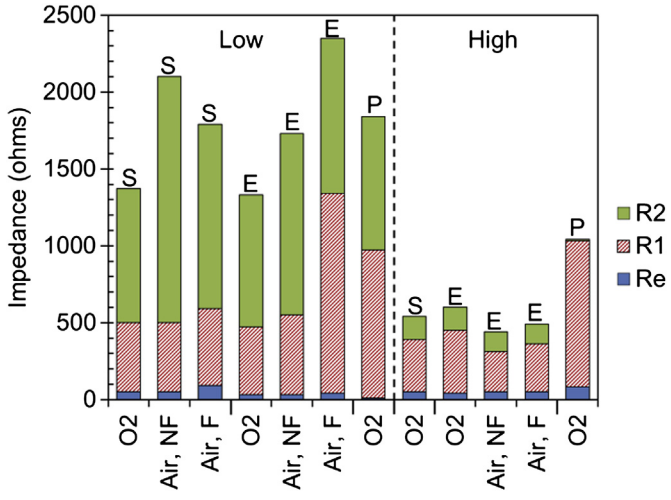

Fig. 11. Comparison of different process impedances for cathodes fabricated by different techniques. S = soaked DC; E = embedded DC; P = PTFE; NF = no flow; N = flow; Low = low current density; High = high current density.

pure oxygen without convective flow, air without convective flow, and air with convective flow. The R_e values for these cathodes range from 10 to 80 Ω and only represent approximately 5% or less of the total impedance. At low discharge current densities, the anode–separator impedance (R_1) is independent of the cathode fabrication technique and the operating gas, with two exceptions. First, for embedded DC cathodes, R_1 increase by 150% when switching from air without flow to air with flow. The dramatic increase in R_1 observed with convective air flow may be due to the reaction of the lithium metal anode surface with nitrogen in the air, which is known to occur at room temperature [35]. The lack of any significant change in R_1 with soaked DC cathodes operating on air may be due to the presence of the liquid electrolyte, which may inhibit the lithium–nitrogen reaction. Second, the R_1 values for the PTFE cathodes are almost double that of the DC cathodes. This large increase reflects the use of a different separator-electrolyte, i.e., Celgard-DME compared to PVDF–PC/EC in the DC cathodes.

At low current densities when operating on pure oxygen, the cathode impedance (R_2) is independent of the cathode fabrication technique. R_2 increases with decreasing oxygen concentration, as expected, due to increases in the kinetic and mass transfer resistances. However, the use of convective air flow improves oxygen mass transfer and reduces R_2. The DC and PTFE cathodes have very different structures and the similar values of R_2 in these cathodes suggest that the controlling mechanism in the cathode at low discharge current densities must be similar. Embedded DC cathodes have lower values of R_2 compared to soaked DC cathodes, which helps explain the improved performance observed in discharge capacity and peak power.

At high discharge current densities, R_1 is reduced compared to the low current density values, and is still independent of the cathode fabrication technique and the operating gas. Note that the large increase in R_1 observed with embedded DC cathodes operating with convective air flow at low current densities is not observed at high current densities. In fact, the R_1 values for the embedded DC cathodes and the soaked DC cathodes are essentially equivalent regardless of the operating gas. The higher current density may be exposing fresh lithium metal surface faster than the nitrogen can react, resulting in the nearly equivalent R_1 impedances. For the PTFE cathodes, the value of R_1 is equal at low and high current densities.

At high discharge current densities, R_2 is substantially reduced due to the reduction in the charge transfer resistance as the overpotential is increased, similar to observations in PEM fuel cell cathodes. R_2 is also independent of the cathode fabrication technique and the operating gas at high discharge current densities. Because the R_2 values are independent of oxygen concentration at high current density, the R_1 impedance must be controlling the discharge reaction. As shown in Fig. 11, the anode–separator impedance is indeed 2× greater than the cathode impedance at a high current density. For the PTFE cathodes, the cathode impedance is extremely small and may explain the high discharge current densities achieved with this cathode.

As an alternative to organic carbonate-based solvents, the impedance of an embedded DC cathode using an RTIL-based electrolyte, 0.5 M LiTFSI in EMITFSI, is also shown in Fig. 7, since this electrolyte showed no evaporation when exposed to convective air flow. Although a direct comparison between the RTIL and soaked DC cathodes is not possible because the current densities are different, 0.04 mA cm^{-2} and 0.1 mA cm^{-2}, respectively, a brief comparison of the R_1 and R_2 impedances is instructive. The higher R_1 value of RTIL cathodes compared to soaked DC cathodes is most likely due to the lower LiTFSI salt concentration and the higher viscosity of RTIL, both of which would increase the ionic transfer resistance. The higher R_2 value in RTIL is most likely due in part to

the lower current density used in the impedance measurement and also to the lower oxygen solubility in RTIL. These data suggest that the RTIL performance could be significantly improved by using ionic liquids with higher salt solubility, lower viscosity, and higher oxygen solubility. Note that EMI and PC, compounds with large positive charges on carbon or nitrogen atoms, are susceptible to nucleophilic attack by the superoxide ion produced during discharge and should not be used in lithium-air cells. A possible alternative could be *N*-methyl-*n*-propylpiperidium [36]. Given the wide range of chemistries available for RTILs, further research is warranted in this area.

The C_2 capacitances as a function of the cathode fabrication technique are shown in Fig. 12 at a low discharge current density of 0.1 mA cm^{-2} using oxygen. The C_2 values for DC cathodes are approximately 40% larger than those for the SC or PTFE cathodes. Because C_2 is proportional to the electrochemically active area of the cathode, the larger capacitance indicates a larger electrochemically active area for embedded DC cathodes. The larger active area explains the higher capacity and peak power performance observed for DC cathodes compared to SC cathodes in Tables 1 and 2. Note that while the real impedance values vary with experimental conditions, the C_2 capacitance values do not.

3.4.3. OCV vs. discharge EIS

To accurately determine the controlling impedances in a cell, the impedance should be measured during discharge, not at open circuit. In Fig. 13, the measured EIS data for embedded DC cathodes are shown at open circuit voltage (OCV) and during a discharge at a high current density. In these experiments, the cell is alternately at open circuit or under load; one cycle is equivalent to OCV for 37 min followed by a discharge at 0.6 mA cm^{-2} for 37 min.

At OCV, R_t increases with depth of discharge, as expected and in agreement with the literature [25–27]. R_t is dominated by the R_2 impedance in the cathode at OCV, while R_e and R_1 contribute less than 1% and 5%, respectively, to the total impedance. In contrast, during a high current density discharge, the total impedance is dominated by the anode–separator interface, R_1. Under load during the first 5 cycles, the value of R_t is nearly constant because R_1 is decreasing while R_2 is increasing. Only during the last 2–3 cycles during discharge does R_2 increase significantly and become comparable in value to R_1. The increase in R_2 is clearly reflected in R_t, especially during the last few cycles. The values of R_1 at OCV and during discharge are essentially equivalent, while the values of R_2 at OCV are 10× greater than during discharge. The OCV data predict that the cathode is controlling the discharge, while the high current density data show that ionic transfer at the anode–separator interface is controlling the discharge. These results clearly show that the OCV impedance data cannot be used to identify the controlling processes during actual discharge.

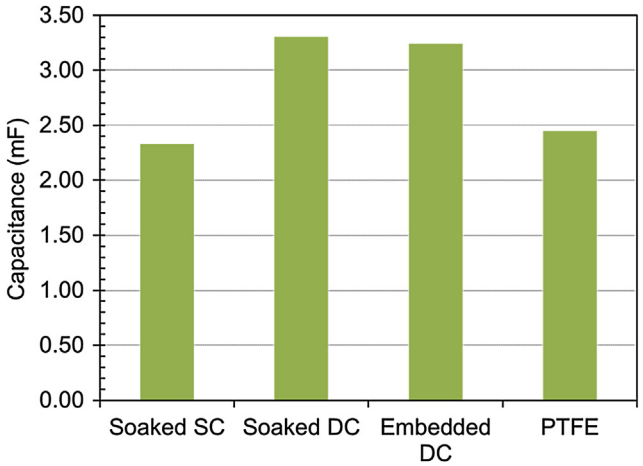

Fig. 12. Capacitance values for cathodes from different fabrication techniques at low discharge current density.

3.4.4. Discharge Impedance measured at low and high current densities

The major impedance controlling discharge depends on the level of the discharge current density. The measured EIS data for embedded DC cathodes are shown in Fig. 14 at a low and a high discharge current density. In these experiments, one cycle equals a discharge for 23 min at 0.6 mA cm^{-2} followed by a discharge for 23 min at 0.1 mA cm^{-2}. As shown in Fig. 14, R_t decreases significantly as the current density increases due to a decrease in the charge transfer resistance (R_2) at higher overpotentials. This is consistent with observations in PEM fuel cell cathodes. At low current densities, the anode–separator interface (R_1) and the cathode (R_2) account for 40% and 60%, respectively, of the total impedance. In contrast, at high current densities, R_1 and R_2 account for 60% and 30%, respectively, of the total impedance. These results are consistent with Tafel slope data which show that kinetic, ionic, and mass transfer resistances are all significant at these discharge current densities. Charge and mass transfer resistances in the cathode are the dominant resistance at low current densities (see Section 3.4.1), while ionic transfer resistance at the anode–separator interface is the dominant resistance to the discharge reaction at high current densities.

Also shown in Fig. 14, are the values of R_e, R_1, and R_2 as the number of cycles and the depth of discharge increase. Although R_e is independent of the discharge current density, this impedance steadily increases with the depth of discharge due to the decomposition of the carbonate solvents (also observed in data in Fig. 13). These data highlight the sensitivity of EIS to capture small variations in cell impedance. R_1 is slightly lower at higher current densities and decreases slightly with the depth of discharge. This may be due to new anode surfaces being exposed during discharge, which would lower the anode–separator impedance. In contrast, R_2 increases steadily with depth of discharge and is 6–7× lower at higher current densities. The steady increase in R_2 is consistent with the deposition of discharge products in the pore structure of the cathode, while the lower value of R_2 at high current densities is consistent with a reduced charge transfer resistance at the higher overpotential.

4. Discussion

4.1. Automotive applications

For automotive applications, lithium-air cells must achieve the performance targets using convective air flow, based on experience with PEM fuel cells. Solvent evaporation from the cathode is then inevitable using conventional solvents and will eventually reach a level where the ionic conductivity will be reduced and cell performance will be degraded. This work highlights the critical need for a new solvent/electrolyte for automotive applications of lithium-air batteries or a very efficient solvent humidification/recovery system. Increasing the cell back pressure reduces solvent evaporation, but at the expense of increasing the parasitic loads from the air subsystem, reducing vehicle range. An ideal solvent should have a high oxygen solubility to support peak power and a low viscosity to promote ionic transfer. The RTIL data presented in this study show that low volatility is not enough to achieve high performance.

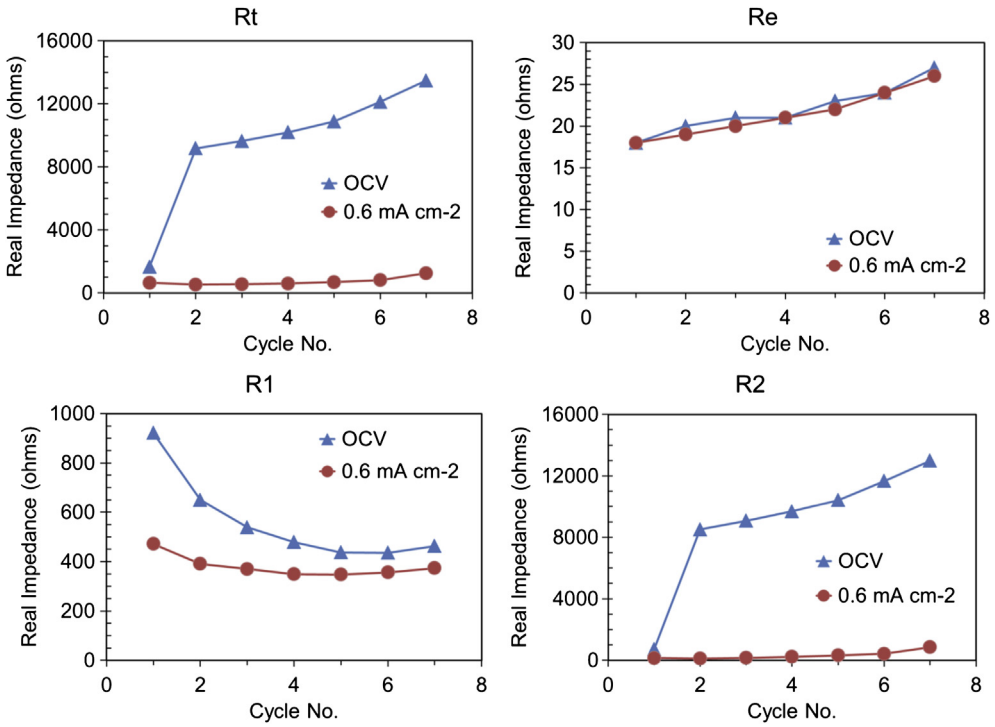

Fig. 13. Impedance data for embedded DC cathodes at OCV and during discharge at a high current density of 0.6 mA cm^{-2}.

Two important automotive targets for EV batteries are the peak power and the specific energy. A minimum peak power is required to support vehicle acceleration for passing, etc. Without sufficient peak power, the size of the battery becomes very large to supply the necessary current and large batteries are difficult to package in a vehicle. The specific energy relates directly to vehicle range. The USABC goals for peak power and specific energy at a C/3 discharge rate are 800 W kg^{-1} and 400 Wh kg^{-1}, respectively, based on total cell mass. As stated previously, the battery must achieve these targets while operating on air, not pure oxygen.

For the embedded electrolyte DC cathodes, the peak power is 4380 W kg^{-1} carbon and the specific energy at a C/3 discharge rate

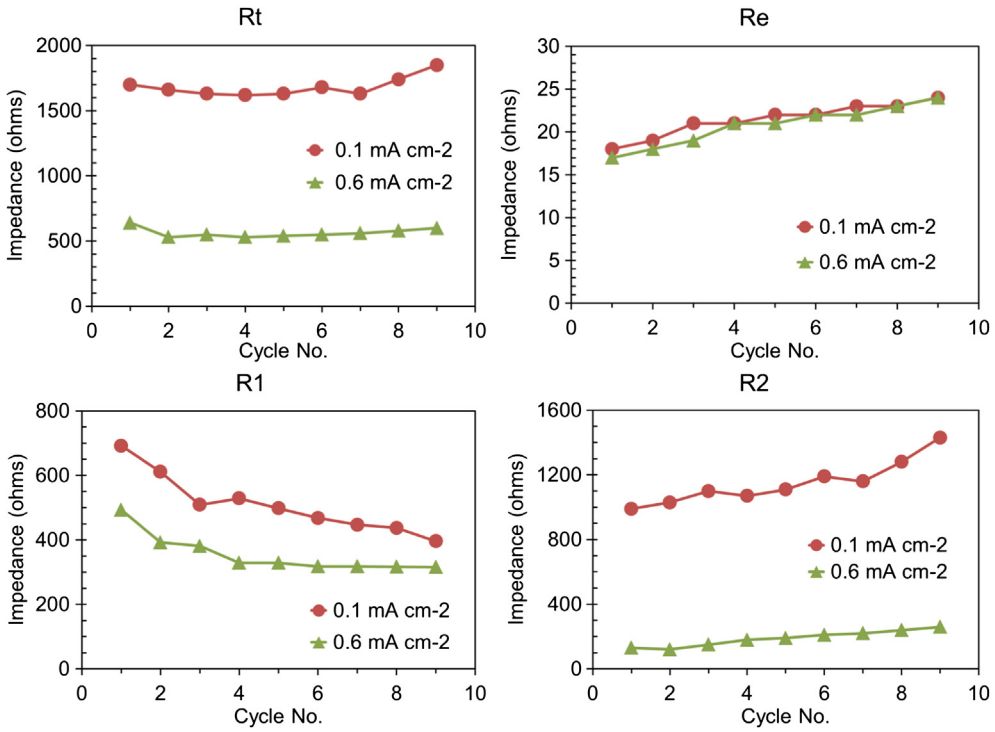

Fig. 14. Impedance data for embedded DC cathodes during discharge at low and high current densities.

is 1200 Wh kg^{-1} carbon when operating on flowing air. In a previous publication [9], the cathodic mass of a lithium-air bipolar plate cell is estimated to be approximately one-third of the total cell mass. In the embedded DC cathodes, the carbon mass is 12% of the cathodic mass. Using the above data, the estimated peak power of cells using embedded DC cathodes is 170 W kg^{-1} cell, and the estimated specific energy is 50 Wh kg^{-1} cell.

To put these results in perspective, the specific power and energy of cells using various cathodes tested in this work are compared to various lithium-ion batteries and the USABC target in Fig. 15. Not surprisingly, the performance of lithium-air cells is lower than lithium-ion batteries and almost an order of magnitude lower than the USABC goal. Also shown in Fig. 15, is the modeled performance of a lithium-air bipolar plate cell design, which shows that the USABC target can be surpassed if the power of the cell can be significantly improved [9]. This work shows that significant performance is possible while operating on air by engineering the cathode structure, but further research in materials, electrolytes, and electrode engineering are required to achieve automotive performance targets.

4.2. Electrochemical analyses

4.2.1. Tafel slopes and reaction orders

The measurement of Tafel slopes and reaction orders are a relatively simple, but highly informative set of experiments. For the first time, the discharge reaction in lithium-air cells is shown to be divided into two regions, one controlled by only kinetic resistance at very low currents and one controlled by kinetic, ionic, and mass transfer resistances at higher currents. The kinetic-only region extends up to current densities of 0.08 mA cm^{-2}. For the majority of the experiments in this work and in the literature, the current densities place the discharge reaction in the region controlled by kinetic, ionic, and mass transfer resistances. Because all three resistances can be significant in magnitude, EIS is used to identify which of these resistances is governing the discharge reaction under specific operating conditions.

4.2.2. EIS results

The most practiced method of EIS data analysis involves proposing an equivalent circuit model, consisting of resistors, capacitors, and other elements combined in series and parallel configurations. The circuit model elements are arranged to reflect the physical reality of the system under study as closely as possible. The model parameter values (resistance, capacitance, etc.) are fit to the EIS data by performing a complex nonlinear least-squares regression analysis. However, the response of a given equivalent circuit model is not unique (i.e., two physically different models can fit the data equally well) and not all electrochemical processes can be reduced to simple circuit elements such as capacitors and resistors. In addition, the results of the regression analysis will depend on proper selection of measurement frequencies, and the existence of noise and bias errors in the data.

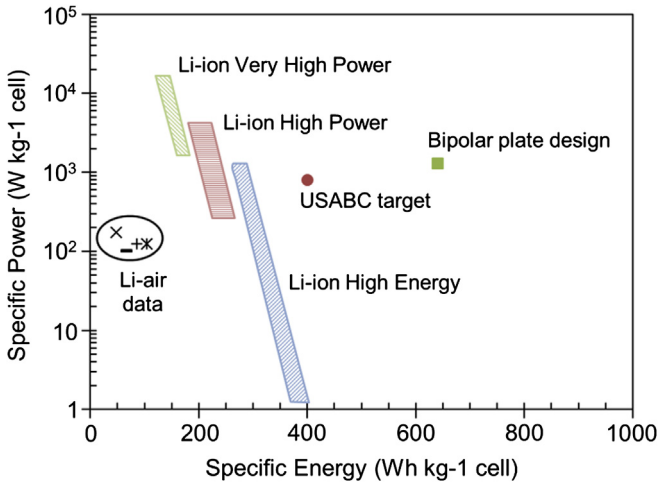

Fig. 15. Comparison of lithium-air data in this work with lithium-ion batteries, USABC target, and modeled bipolar plate cell design.

In this paper, EIS is used to aid in the interpretation of the performance of lithium-air cathodes fabricated by different techniques. The EIS data and analyses apply only to the discharge performance. Because the goal is not to develop an equivalent circuit model of the lithium-air cell, the graphical analysis technique is used as a simple method to extract the impedance and capacitance values for each distinct element. To verify the validity of this method, electronic test circuits with known resistance and capacitance elements have been reconstructed using the graphical technique (data not shown).

The measurement of EIS data at OCV does not provide information on what is controlling the discharge reaction rate. While the OCV EIS data predicts that the cathode is controlling the discharge rate with essentially no contribution from the anode–separator interface, EIS data collected during discharge clearly shows that the cathode and the anode–separator interface are both significant in controlling the discharge rate. The EIS measurements made during discharge provide accurate information on what is controlling the discharge reaction rate and also show how the relative magnitudes of cathode and anode–separator impedances shift with increases in current density and the depth of discharge. Based on impedance data taken at different salt concentrations, the ionic transfer resistance appears to be mainly in the anode–separator interface, while the cathode contains the kinetic and mass transfer resistances. At low current densities, the cathode impedance controls the discharge reaction and is dependent on the oxygen concentration. In contrast at high current densities, the anode–separator impedance controls the discharge reaction and the cathode impedance is independent of the oxygen concentration. Improving ionic transfer at the anode–separator interface and mass transfer in the cathode will be critical to engineering a better performing lithium-air cell.

A mass transfer limited response (Warburg effect) is not observed in the Nyquist plots at low frequencies, even at low oxygen concentrations. Although a Warburg effect is expected based on the Tafel slope results, several factors can explain this. First, the cathode structure does not resemble a planar electrode in a semi-infinite electrolyte, i.e., some parts of the electrode are always in contact with a significant oxygen concentration. Second, the noise levels in the low frequency data are large in some experiments and may mask the effect. Finally, high capacitance values can mask the mass transfer response in porous electrodes.

A 45° line at high frequencies is observed in some Nyquist plots, indicative of significant ionic transfer resistance. While not observed in all EIS data sets, these data are consistent with the Tafel slope, reaction order, and EIS data, which show that ionic transfer resistance is important.

4.3. Summary

For automotive applications, lithium-air batteries still require significant improvements. The SOA performance places the technology far outside the requirements for use in EVs, particularly in terms of cycle life, specific energy, and peak power. The cathode fabrication results coupled with the Tafel slope and EIS data show

how cell performance can be improved and significant progress in understanding the discharge reaction developed using existing material sets and analysis techniques. The understanding and design improvements developed here should be applicable to the next generation of materials. While the results apply only to the particular cathodes of this study, the analysis techniques described herein should be applicable to any lithium-air cell designs.

References

[1] K.M. Abraham, Z. Jiang, J. Electrochem. Soc. 143 (1996) 1.
[2] J. Read, J. Electrochem. Soc. 149 (2002) A1190–A1195.
[3] S. Zhang, D. Foster, J. Read, J. Power Sources 195 (2010) 1235–1240.
[4] A. Dobley, C. Morein, K.M. Abraham, 208th ECS Meeting (2005) #323.
[5] J. Zheng, D. Wang, W. Xu, J. Xiao, R.E. Williford, J. Power Sources 195 (2010) 4332–4337.
[6] T. Ogasawara, A. Debart, M. Holzapfel, P. Novak, P. Bruce, J. Am. Chem. Soc. 128 (2006) 1390–1393.
[7] A. Debart, J. Bao, G. Armstrong, P. Bruce, J. Power Sources 174 (2007) 1177–1182.
[8] J. Read, J. Electrochem. Soc. 150 (2003) A1351–A1356.
[9] J. Adams, M. Karulkar, J. Power Sources 199 (2012) 247–255.
[10] USABC Goals for Advanced Batteries for EVs, Energy Storage System Goals (October 14, 2010). http://www.uscar.org/guest/teams/12/U-S-Advanced-Battery-Consortium.
[11] A.S. Arico, V. Antonucci, V. Alderucci, E. Modica, N. Giordano, J. Appl. Electrochem. 23 (1993) 1107–1116.
[12] Y. Bultel, L. Genies, O. Antoine, P. Ozil, R. Durand, J. Electroanal. Chem. 527 (2002) 143–155.
[13] G. Dotelli, L. Omati, P.G. Stampino, P. Grassini, D. Brivio, J. Power Sources 196 (2011) 8955–8966.
[14] I.D. Raistrick, Electrochim. Acta 35 (1990) 1579–1586.
[15] M.B. Ji, Z.D. Wei, S.G. Chen, M.R. Xia, Q. Zhang, X.Q. Qi, X.H. Hu, W. Ding, L. Li, Electrochim. Acta 56 (2011) 4797–4802.
[16] R. Makharia, M.F. Mathias, D.R. Baker, J. Electrochem. Soc. 152 (2005) A970–A977.
[17] D.B. Zhou, H. Vander Poorten, Electrochim. Acta 40 (1995) 1819–1826.
[18] Y. Bultel, K. Wiezell, F. Jaouen, P. Ozil, G. Lindbergh, Electrochim. Acta 51 (2005) 474–488.
[19] F. Jaouen, G. Lindbergh, K. Wiezell, J. Electrochem. Soc. 150 (2003) A1711–A1717.
[20] F. Jaouen, G. Lindbergh, J. Electrochem. Soc. 150 (2003) A1699–A1710.
[21] S.-J. Lee, S.-I. Pyun, Electrochim. Acta 52 (2007) 6525–6533.
[22] S.-J. Lee, S.-I. Pyun, J. Electrochem. Soc. 155 (2008) B1274–B1280.
[23] M.C. Lefebvre, R.B. Martin, P.G. Pickup, Electrochem. Solid-state Lett. 2 (1999) 259–261.
[24] A. Lasia, J. Electroanal. Chem. 397 (1995) 27–33.
[25] M. Eswaran, N. Munichandraiah, L.G. Scanlon, Electrochem. Solid-state Lett. 13 (2010) A121–A124.
[26] P. Kichambare, J. Kumar, S. Rodrigues, B. Kumar, J. Power Sources 196 (2011) 3310–3316.
[27] M. Mirzaeian, P.J. Hall, J. Power Sources 195 (2010) 6817–6824.
[28] F. Mizuno, S. Nakanishi, Y. Kotani, S. Yokoishi, H. Iba, Electrochemistry (Japan) 78 (2010) 403–405.
[29] B.D. McCloskey, D.S. Bethune, R.M. Shelby, G. Girishkumar, A.C. Luntz, J. Phys. Chem. Lett. 2 (2011) 1161–1166.
[30] S.A. Freunberger, Y. Chen, Z. Peng, J.M. Griffin, L.J. Hardwick, F. Barde, P. Novak, P.G. Bruce, J. Am. Chem. Soc. 133 (2011) 8040–8047.
[31] USABC Electric Vehicle Test Procedures Manual, Revision 2, Appendix I, Derivation of USABC Battery Peak Power Calculations. USABC Manuals. http://www.uscar.org/guest/teams/12/U-S-Advanced-Battery-Consortium.
[32] M.E. Orazem, B. Tribollet, Electrochemical Impedance Spectroscopy (The ECS Series of Texts and Monographs), Wiley Publishing, New Jersey, 2008.
[33] B.E. Conway, J. Electrochem. Soc. 138 (1991) 1539–1548.
[34] M. Gaberscek, J. Moskon, B. Erjavec, R. Dominko, J. Jamnik, Electrochem. Solid-state Lett. 11 (2008) A170–A174.
[35] M. Wu, Z. Wen, Y. Liu, X. Wang, L. Huang, J. Power Sources 196 (2011) 8091–8097.
[36] Y. Katayama, H. Onodera, M. Yamagata, T. Miura, J. Electrochem. Soc. 151 (2004) A59–A63.